JOURNAL OF GEOPHYSICAL RESEARCH, VOL. 115, F03042, doi:10.1029/2009JF001515, 2010

Measurement of the deformation field associated with fracture propagation in weak snowpack layers

A. van Herwijnen,[1] J. Schweizer,[1] and J. Heierli[2,3]

Received 4 September 2009; revised 11 May 2010; accepted 25 May 2010; published 29 September 2010.

[1] Dry snow slab avalanches release as a result of the failure of a weakly bonded layer located below a slab-like layer of cohesive snow. Traditionally the failure of the weak layer was attributed to the formation and propagation of volume-conserving simple shear cracks. Over the past decade, however, evidence for slope-normal subsidence associated with fracture propagation in snow has accumulated, pointing toward a new understanding of fracture propagation in snow. The typically very high porosity of weak layers implies a loss of volume during fracture, as the aggregate of ice grains composing the weak layer collapses and rearranges in a tighter packing order. Therefore, in the new models failure is attributed to the formation and propagation of mixed-mode anticracks. In order to experimentally investigate the nature of the deformation field associated with fracture propagation through weak snowpack layers we monitored propagating fractures in field tests on natural snowpacks with a high level of detail using high-speed photography and analyzed the data with particle tracking velocimetry. The collapse of the weak layer was always observed and ranged between 0.3 cm and 4 cm. In all experiments the collapse was found to coincide with the fracture front. A shear crack preceding the collapse front was not detected at any stage of the process. It is concluded that the volumetric collapse of the weak layer, which is characteristic of anticracking, is the rule rather than the exception for the fracture process in stratified snow and therefore for slab avalanche release.

Citation: van Herwijnen, A., J. Schweizer, and J. Heierli (2010), Measurement of the deformation field associated with fracture propagation in weak snowpack layers, *J. Geophys. Res.*, *115*, F03042, doi:10.1029/2009JF001515.

1. Introduction

[2] Dry snow slab avalanches release as a result of the extended failure of a weak snowpack layer, located below a slab-like layer of well-bonded snow [e.g., *Perla and LaChapelle*, 1970; *Schweizer et al.*, 2003]. Typically, weak layers are extremely porous and therefore the process leading to their failure differs from that of dense geomaterials, mainly due to the possibility of a tighter rearrangement of grains in the course of fracture.

[3] The deformation and failure of porous materials is a recurrent theme in geophysics. For instance, *Katsman and Aharonov* [2006] investigated the formation of compaction bands from crack-like structures by grain crushing in the presence of compressive stress. *Sternlof et al.* [2005] associated localized compaction in porous sandstone with a contractile Eshelby inclusion and approximated the incurring stress field by anticrack fields as introduced by *Fletcher and Pollard* [1981]. In this context, the term anticrack refers to a fracture mode in which the displacement field is equal in magnitude but opposite in sign to that of a classical tensile crack. Consequently, anticracks can propagate under compression.

[4] For many years, the role of volume change during the fracture of weak snowpack layers has not been taken into account. Until recently, the criterion for fracture propagation was formulated in terms of a volume-conserving shear fracture model, in which cracking in simple shear was supposed to release the energy for fracture propagation [e.g., *McClung*, 1979]. Over the past decade however, evidence for slope-normal deformation associated with fracture propagation in snow has accumulated, pointing toward a new understanding of the fracture process in snow.

[5] On the practical side, *Duclos* [1999] and *Jamieson and Schweizer* [2000] provided evidence for the volumetric collapse of buried weak layers and the latter suggested that the collapse may release potential energy contributing to the propagation of fracture. The first direct measurement of the collapse process was performed by *Johnson et al.* [2004]. An array of geophones was placed on the snow surface over low angle terrain. Fracture was then triggered artificially by stepping over the surface. The motion caused by the passing fracture front was recorded by the geophones. The analysis

---

[1] WSL Institute for Snow and Avalanche Research SLF, Davos-Dorf, Switzerland.

[2] Institut für Zuverlässigkeit von Bauteilen und Systemen, Karlsruher Institut für Technologie, Karlsruhe, Germany.

[3] Fraunhofer-Institut für Werkstoffmechanik IWM, Freiburg, Germany.

0148-0227/10/2009JF001515

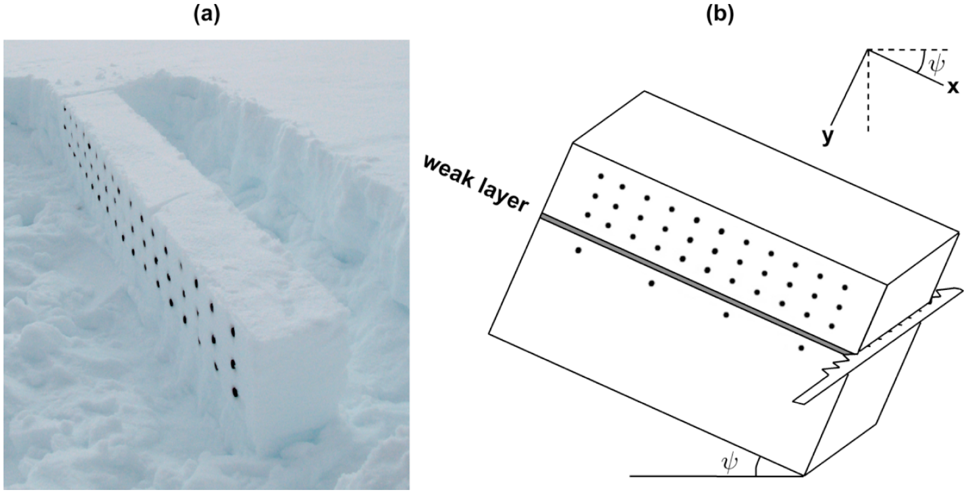

Figure 1. Propagating fractures in weak snowpack layers were photographed in beam tests using a high-speed camera. (a) Photo of an isolated beam with black markers. (b) Schematic drawing of the test procedure and coordinate system used in the image analysis.

of the arrival times at different geophones indicated a fracture propagation velocity of about 20 ms^{-1}. Using high-speed photography, *van Herwijnen and Jamieson* [2005] later recorded the displacements associated with fracture propagation in weak snowpack layers with submillimeter resolution. These experiments were carried out for various types of weak layers and loading conditions. Again, the velocity of fracture propagation was found to be on the order of a few tens of meters per second and collapse of the weak layer was consistently observed.

[6] On the theoretical side, the stability of a weak snowpack layer under compressive and mixed-mode loading conditions was analyzed by *Heierli and Zaiser* [2006, 2008] and by *Heierli et al.* [2008]. The calculations take into account the amount of work done by compressive loads when slope-normal displacement of the slab is permitted by the crushing of the weak layer (by contrast, no work is done by compressive loads under volume-conserving simple shear cracking). The calculations indicate that, while for crack nuclei and small cracks, the displacement field is similar to that of Fletcher-type anticracks, for long cracks the limited amplitude of the slope-normal displacement results in a characteristic nonlinear, kink-shaped bending wave [*Heierli et al.*, 2008]. The physics of these nonlinear waves has been analyzed by *Heierli* [2005], in which the asymptotic state of the disturbance afar from the trigger point is calculated.

[7] The aim of this paper is to experimentally investigate the nature of the deformation field associated with fracture propagation through weak snowpack layers and to provide evidence whether the collapse is the actual carrier for fracture propagation in snow or whether a simple shear crack precedes it. To achieve this, the fracture process was photographed in situ using a high-speed camera. Detailed displacement fields are obtained from the beginning to the end of the process.

2. Method

[8] The present study uses a field test developed by *Gauthier and Jamieson* [2006] and *Sigrist and Schweizer* [2007] and validated by *Gauthier and Jamieson* [2008]. The field test is appropriate to study fracture propagation. A large rectangular section of snow containing a weak layer was isolated from the surrounding snowpack, exposing a cross section of the snow stratification (Figure 1). To enhance the visualization of the deformation, numerous black markers were inserted in a grid-like pattern on the exposed cross section of the column both above and below the weak layer. The fracture process was then triggered by cutting the weak layer with a snow saw (2 mm thick), starting from the down-slope end of the beam and sawing until a self-propagating fracture started (Figure 1b). The fracture process was then visible on the exposed cross section and recorded using a high-speed camera. The length of the saw cut at which fracture starts propagating, i.e., the critical cut length r_c, was measured with a ruler.

[9] The experiments were performed on low angle slopes between 0° and 19°. On steep slopes, typically slopes steeper than 30°, the slab starts sliding in accelerated motion after the fracture has propagated from one end of the weak layer to the other [*van Herwijnen and Heierli*, 2009]. This motion superposes the displacements caused by weak layer fracturing [*van Herwijnen and Jamieson*, 2005]. The experiments were therefore carried out on low angle slopes, on which the slab rapidly comes to rest.

[10] The deformation of the slab above the weak layer was analyzed using Particle Tracking Velocimetry (PTV). PTV is a technique widely used in fluid mechanics, in which displacement and velocity fields are measured indirectly by means of tracer particles. The technique has the advantage of being largely nonintrusive and being capable of simultaneously measuring the state of deformation over an entire cross section of the sample. PTV has previously been used to study the deformation and failure of snow in snow stability tests [*Schweizer et al.*, 1995]. *Gleason* [2004] used PTV to measure the deformation of snow under compression, showing the bridging effect of hard snow layers. *van Herwijnen and Jamieson* [2005] used PTV to analyze fracture propagation of weak snowpack layers.

[11] The current study is based on field work carried out in the Swiss Alps near Davos, Switzerland between January 2008 and March 2009. The field samples cut out for the experiment were 0.3 m wide in the cross-slope direction and between 3 m to 4 m long in down-slope direction, with slope-normal faces on the lower and upper ends. Four experiments were carried out on slopes with weak layers consisting of either buried surface hoar (SH) or faceted crystals (FC). At each test site, a snow profile was taken to gather information on hardness, crystal type, crystal size, thickness, temperature and density of each layer, according to the guidelines of the *Canadian Avalanche Association* [2002].

2.1. High-Speed Photography

[12] The high-speed camera VDS Vosskühler HCC-1000 used in the present study is suitable for field work. The camera has a resolution of 1024 by 512 effective pixels. Images were recorded at a rate of approximately 300 frames per second (fps), depending on aperture and shutter speed. The device can store a sequence of 1024 images preceding a trigger signal, which was given manually soon after termination of the fracture process. The camera was mounted on a tripod and aimed approximately perpendicular to the exposed cross section of the sample.

2.2. Particle Tracking

[13] Particle tracking software [*Crocker and Grier*, 1996] was used to analyze the images of the video sequence from the fracture process. A band-pass filter was used to identify the images of the markers by searching for a local brightness minimum. Pixel coordinates were assigned to the centroid of each marker image. This procedure was repeated for each marker on all the frames in the video sequence so that at any recorded time the position of all the markers was determined. The set of the centroid coordinates for each marker thus represents the trajectory of the deformation at the corresponding point.

[14] The motion of the markers was analyzed using a coordinate system as defined in Figure 1b: the x axis pointing in down-slope direction parallel to the snow surface, the y axis pointing toward the ground normal to the snow surface. Displacements in the z axis parallel to the optical axis of the camera were considered to be negligible and were not taken into account. The instant displacements $u_x(t)$ and $u_y(t)$ of each marker were measured with reference to the initial positions x_0 and y_0 of each marker before fracture. The initial position was obtained by averaging the positions of each marker over 50 frames prior to movement, in order to remove small fluctuations in the static position of the marker, e.g., due to thermal fluctuation in the CCD array or small changes in illumination.

[15] The instant velocities $v_x(t)$ and $v_y(t)$ of each marker were obtained by numerical derivation of $u_x(t)$, and $u_y(t)$ using the first-order forward scheme, e.g., $v_x(t) = [u_x(t + \Delta t) - u_x(t)]/\Delta t$ where Δt is the time interval between two subsequent frames.

[16] The accuracy of the particle tracking software depends on the size and the quality of the images, i.e., signal-to-noise ratio, and determines the smallest displacement that can be observed. The choice of the magnification is a trade-off between the size of the field of view (FOV), the image contrast and the apparent particle size, i.e., the size of the markers in the digital images. For a low magnification, i.e., small apparent particle size, the field of view is increased at the expense of image contrast and signal-to-noise ratio. For this study, the field of view was typically around 3 m and the marker diameter was approximately 25 pixels. The accuracy for static markers was determined for each experiment by calculating the standard deviation in the initial position of the markers, i.e., 50 frames prior to movement. The typical accuracy was on the order of 0.05 pixels.

[17] In order to convert the measured displacements in pixels into distances in centimeters a conversion factor was determined for each video sequence. This was done by measuring a reference distance between two markers with a ruler prior to carrying out the fracture experiment. The distance was measured between the first and the last marker in one row of markers with a measurement error of 1 cm. For the video sequences analyzed in this study, the conversion factor was around 0.3 cm/pixel, resulting in a typical measurement error of 0.2 mm.

2.3. Correcting for Digital Image Distortion

[18] As the focal plane of the camera lens system is not entirely planar, a slight barrel distortion of the image occurs. In order to remove this systematic error a photograph of a regular grid of markers was used to construct an empirical distortion model. The distance between the markers closest to the center of the image, where image distortion can be neglected, was used to scale the image. By comparing the measured distance of the markers to the center of the image with the actual distance, the distortion of the image was obtained. The image distortion was removed using an empirical third-order polynomial fit between the actual and measured distance of the pixels. The systematic error in the position of the markers did not exceed 2% in our experiments.

2.4. Refinement of Trajectories

[19] Pixel clipping at the perimeter of the marker images introduces scatter in the displacement data. Pixel clipping occurs when the edge of a marker image crosses a pixel boundary, causing a jump in the estimation of the centroid coordinates. The lower the resolution of the images, the more this problem contributes to the uncertainty of the marker position [*van Herwijnen and Jamieson*, 2005]. In the present study, pixel clipping only occurred for a few markers in areas with uneven illumination, typically the corner of the sample where the fracture was initiated with the saw cut. In order to eliminate these artifacts a filtering method was developed.

[20] Two types of artifacts due to pixel clipping are distinguished. First, when the edge of a stationary marker image was located between two adjacent pixels, static pixel clipping occurred. This caused the calculated position of the centroid of a marker to fluctuate between two values as is visible between t = 0 and t = 0.22 s in Figure 2a (part i). Second, during the passage of the fracture, the image of the marker moved, and kinematic pixel clipping caused sudden

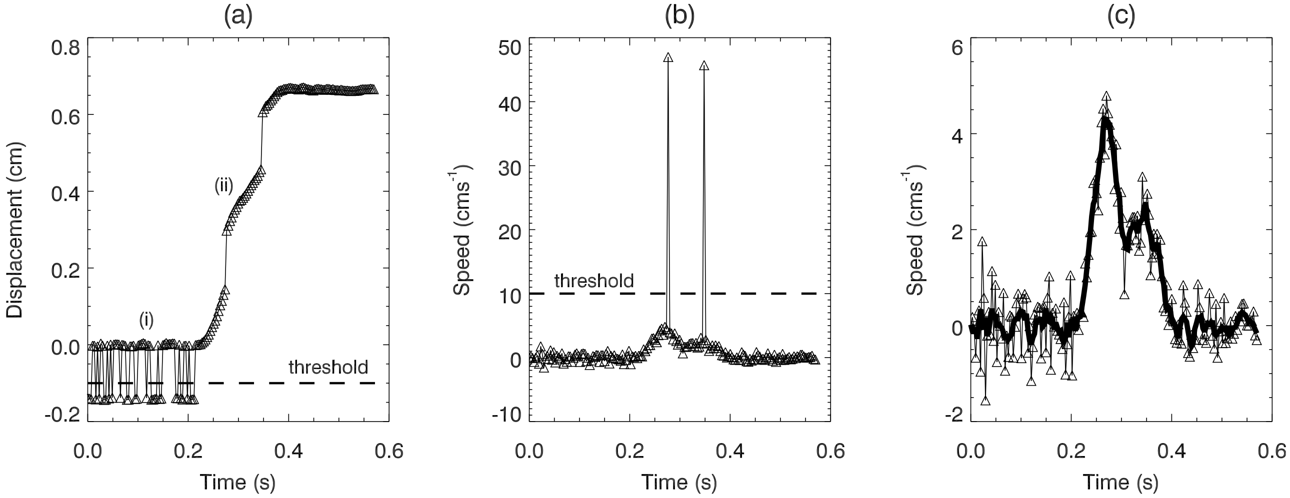

Figure 2. Filtering method used to remove artifacts due to pixel clipping. (a) Example of a trajectory exhibiting static (part i) and kinematic pixel clipping (part ii). The triangles represent the centroid of the marker in each frame. A suitable threshold value was chosen to separate data points to correct for static pixel clipping. (b) To correct for kinematic pixel clipping, a threshold value was used to identify spikes in the marker velocity. (c) Smoothed marker speed after applying a five-pointmoving average filter (thick line).

jumps in the centroid position, as visible at $t = 0.27$ s and $t = 0.34$ s in Figure 2a (part ii).

[21] Static pixel clipping was eliminated by separation. A threshold value lying between both position estimates was chosen to separate the two populations of positions (Figure 2a). The larger population was assumed to represent the correct position and the smaller population the erroneous position. Erroneous positions were then matched with the mean of the population classified as correct, thereby removing the scatter in the trajectory.

[22] Kinematic pixel clipping was eliminated by using the fact that a jump in the displacement corresponds to a sharp peak in the velocity of the marker image, with amplitude much larger than the velocity of the marker caused by the actual motion. These peaks were identified by manually choosing a suitable threshold value determined individually for each trajectory (Figure 2b). The absolute values of the x and y components of velocity were used in order to account for pixel clipping in all directions. Data points that fell above the threshold were classified as erroneous and assigned a new value equal to the average velocity of the two closest valid data points. Fluctuations in the velocity were further reduced by taking the moving average over five data points, which was found to be most effective without substantial loss of detail (Figure 2c). This smoothing operation

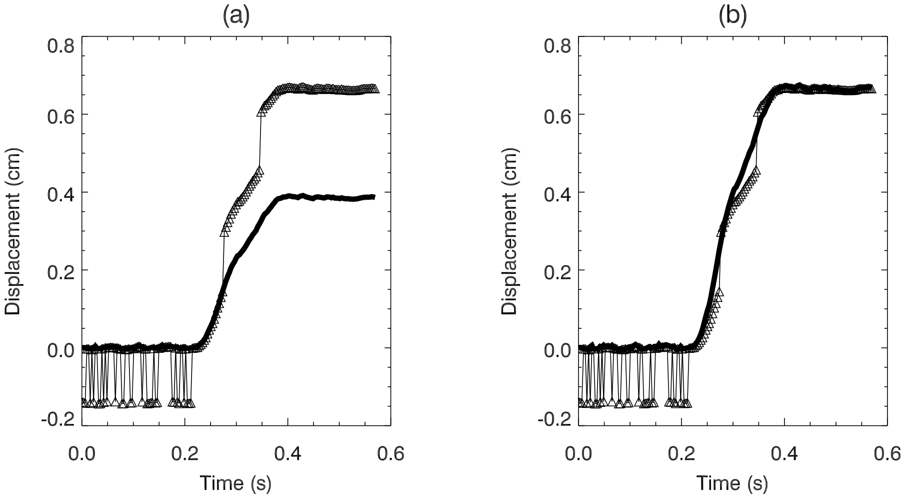

Figure 3. Example of trajectory refinement (solid lines) obtained by integrating the smoothed and corrected marker speed (Figure 2c). (a) This procedure results in a lower total displacement compared to the original data (triangles). (b) The refined trajectory is rescaled to match the final displacement.

Table 1. Experimental Parameters and Snow Properties During the Fracture Experiments[a]

Test	ψ (deg)	FOV (cm)	fps	ϵ (cm)	F	H (cm)	h (cm)	ρ (kg m^{-3})	r_c (cm)
A	11	305	307.92	0.02	SH	38 (−13, 8, 21)	4	250	16
B	11	305	307.92	0.02	SH	38 (−10, 9, 22)	4	250	19
C	19	280	307.33	0.01	FC	43 (−7, 7, 14, 23, 32)	9	250	44
D	0	300	307.33	0.01	SH	66 (−17, 16, 30, 43, 56)	1	150	28

[a] Here ψ, slope angle in degrees; FOV, field of view of the camera; fps, frame rate of the digital recording; ϵ, uncertainty of position measurement; F, weak layer crystal type; H, depth of weak layer measured vertically (values in parentheses are mean distance to weak layer of rows of markers); h, average weak layer thickness measured vertically; ρ, average slab density above weak layer; r_c, cut length at onset of fracture propagation.

was also performed on trajectories for which pixel clipping did not occur.

[23] The refined trajectory was finally obtained by integration over time of the smoothed and corrected marker velocity data. This operation resulted in a lower total displacement of the markers which exhibited dynamic pixel clipping (Figure 3a). Therefore, the refined trajectory for those markers was rescaled to match the actual total displacement after fracture (Figure 3b).

2.5. Propagation Velocity

[24] As a fracture propagates through the weak layer there is a delay in the onset of the slope-normal displacement of markers located on the same row. The delay in the onset of the slope-normal displacement was used to determine the propagation velocity c. A detailed description of the method used to determine the propagation velocity can be found in the work by *van Herwijnen and Jamieson* [2005].

3. Results

[25] Four experiments in which fracture propagation occurred were recorded according to the method outlined in section 2. The experiments are labeled A, B, C and D. A movie showing experiment A is provided online (Animation 1).[1] An overview of the experimental parameters and snow conditions is given in Table 1.

[26] The experiments labeled A and B were performed on the same day on a sample comprising a weak layer composed of large buried surface hoar crystals (30 to 40 mm). These experiments were performed on a slope with 11° inclination. Three rows of markers were inserted on the exposed cross section, two above the weak layer and one below. Preliminary tests on this layer, which was buried below roughly 20 cm of soft faceted snow (average density of 175 kg m^{-3}), did not result in full propagation of the fracture through the weak layer. Therefore, the load above the weak layer was increased by carefully shoveling 15 cm of compacted snow (average density of 330 kg m^{-3}) on top of the existing slab. The snow was left to settle for a few hours before performing the experiments. Interestingly, with the additional load, the fracture propagated through the whole length of the sample. In addition to this longitudinal propagation, a transverse fracture through the slab, i.e., perpendicular to the direction of weak layer, was observed in both cases roughly halfway through the sample.

[27] The experiment labeled C was performed on a sample comprising a weak layer of faceted crystals (1.5 to 2.5 mm) underlying a thin crust at a depth of 43 cm on a slope with 19° inclination. The experiment labeled D was performed on a weak layer composed of large buried surface hoar crystals (20 to 50 mm) at an average depth of 66 cm. The slab consisted of two distinct layers: 35 cm of fresh snow (average density of 80 kg m^{-3}) overlying 31 cm of dense old snow (average density of 220 kg m^{-3}). The terrain consisted of a shallow convex roll with an average slope angle of 0°. The slope angle varied from 2° at the edge of the beam where the fracture was initiated to minus 2° at the far end of the beam. For both these experiments four rows of markers were inserted in the snow above the weak layer and one row of markers below the weak layer. The fracture propagated through both samples and no transverse fractures through the slab were visible after fracture propagation.

3.1. Displacement

[28] The displacement profile of the slab associated with the fracturing of the weak layer is shown in Figure 4 for experiments C and D. The displacement is for a marker near the center line of the slab (i.e., not in the neighborhood of the weak layer where fracture occurred) and well away from the trigger point. As the weak layer fractured, the slope-normal displacement u_y increased rapidly following a kink-shaped profile. The duration of the motion was less than 0.1 s, after which the normal displacement remained constant. The slope-parallel displacement u_x of the marker, appears to be a superposition of two movements: (1) the back-and-forth oscillation of u_x due to the rotation accompanying the back-and-forth bending of the slab, which is always present, and (2) the slope-parallel translation of the slab (slip), which only appears for larger slope angles. In case C, in which the slope angle was 19°, the superposition of both movements appears as an elbow in the u_x curve. In case D, in which the slope angle was close to 0°, the slip was insignificant and only the rotation (the up-and-down profile of u_x) appears. These displacement profiles are typical for a marker near the center line of the slab. However, to understand the fracture process, we need to examine the deformation field everywhere in the slab above the weak layer and below the weak layer.

[29] The way in which the slope-parallel and slope-normal displacements depend on the vertical position of the markers is shown in detail in Figure 5. The instant slope-parallel displacement was very close to zero at the level of the weak layer (where fracture takes place) and increased closer to the snow surface. By contrast, the instant slope-normal displacement began and evolved in unison, with

---

[1] Animation 1 is available in the HTML.

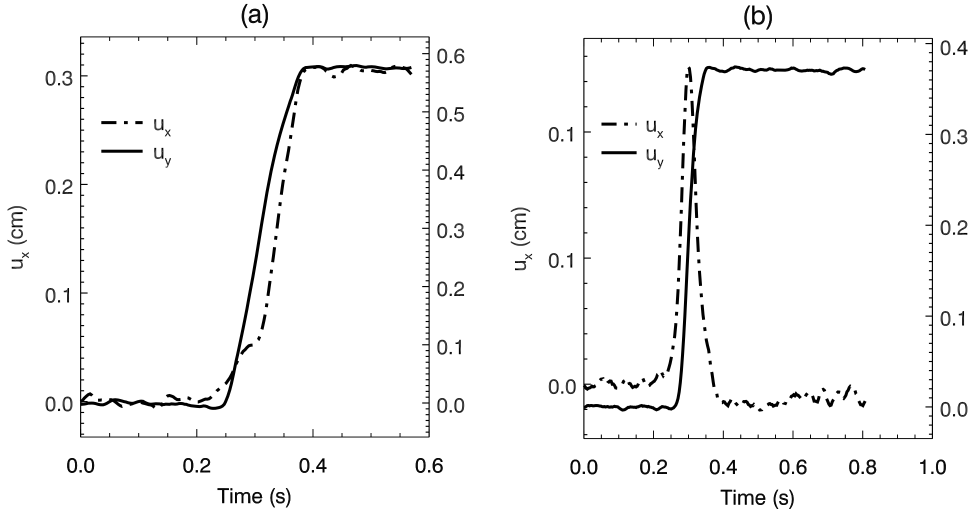

Figure 4. Slope-parallel (u_x, dash-dotted lines) and slope-normal (u_y, solid lines) displacement of a marker positioned on the center line of the beam in (a) experiment C and (b) experiment D. The center line is above the neutral line of the beam due to the increasing density of the snow toward the weak layer.

virtually identical amplitude, independently of the distance of the marker to the weak layer.

[30] As the fracture propagates, the kink-shaped disturbance travels through the slab, which consequently subsides. The evolution of the shape of the disturbance is shown in Figure 6, where the slope-normal displacement of one row of markers in experiment D is shown at eight moments during fracture propagation. Initially, as the fracture started to propagate, the slab lost support and began to move downward (black and blue curves). Soon afterward, the final slope-normal displacement was attained at the trigger side while the far end of the sample was not yet affected (green and yellow curves). Subsequently, the disturbance traveled through the entire sample and exited through the far end (orange and red curves). The kink-like, back-and-forth bending of the slab is clearly evidenced in this graph.

[31] The final displacements both in slope-parallel and slope-normal direction varied from marker to marker. The range of the variation is given in Table 2. In three experiments, cases A, B and C, the final slope-normal displacement decreased with increasing distance from the trigger point. In one experiment, case D, the final slope-normal displacement first decreased then increased with increasing distance from the trigger point. Figures 4 and 7, as well as Table 2, show that both the instant and final displacements were distinctly larger in the slope-normal direction than in the slope-parallel direction.

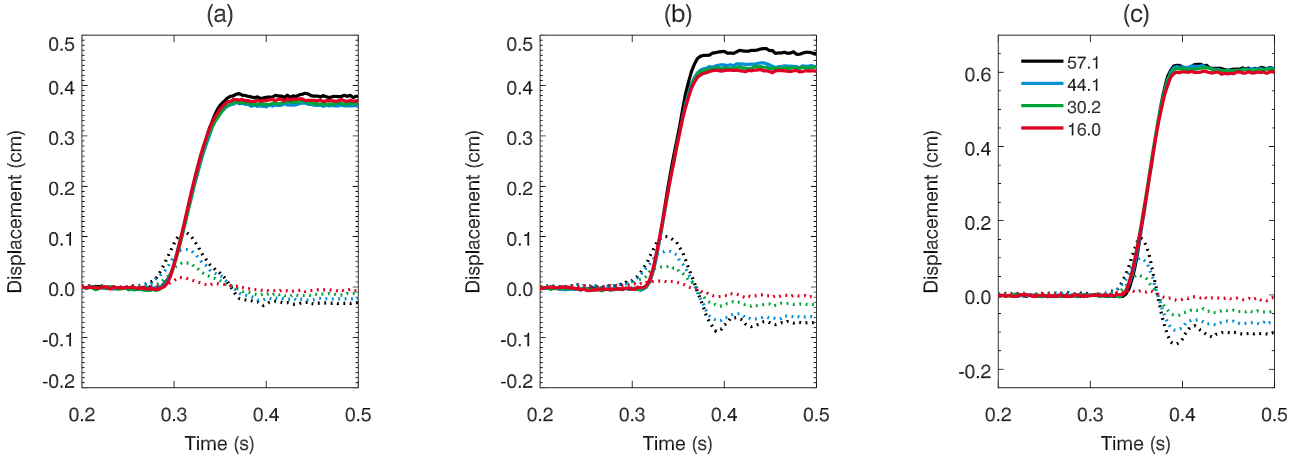

Figure 5. Slope-parallel displacement (dashed lines) and slope-normal displacement (solid lines) in test D as function of time for marker positions at (a) one third, (b) in the middle, and (c) at two thirds of the beam. Each line represents the displacement of one marker. The colors identify makers of different rows but same position along the *x* axis. The vertical distance in centimeters from the markers to the weak layer is indicated in the upper left corner of Figure 5c. Note the different scales on the vertical axis.

Table 2. Measured Displacements and Propagation Velocity[a]

Test	Final u_x (cm)	Final u_y (cm)	c (ms^{-1})
A	1.38–2.07	2.35–4.06	32 ± 2
B	1.38–1.64	2.75–3.47	36 ± 2
C	0.20–0.34	0.51–0.82	27 ± 1
D	−0.15–0.06	0.34–0.70	30 ± 2

[a] Experimental results were obtained from the refined trajectories according to the method outlined in sections 2.2 and 2.3. Final u_x and final u_y, slope-parallel displacement and slope-normal displacement, respectively, measured after fracture; c, observed propagation velocity over entire sample length.

3.2. Collective Motion of Markers

[32] By looking at the velocity profiles of all markers throughout the sample at different times, a collective motion traveling as a stable packet is observed (Figure 8, experiment D). As the fracture propagated, a zone with downward slope-normal motion (right panel) and a zone of back-and-forth slope-parallel motion (left panel) propagated through the slab. The slope-parallel velocities were highest near the snow surface and vanished toward and below the weak layer (left panel). Two extremals of opposing sign are clearly visible on the upper edge. This pattern is characteristic of the back-and-forth bending with instant rotation axis near the weak layer. A collective motion caused by a hypothetical shear crack ahead of the collapse front, which would manifest itself as a peak in the slope-parallel velocities at the weak layer, is not detected at any point. Instead, the slope-parallel velocities vanish in this region.

3.3. Propagation Velocity of the Disturbance

[33] The propagation velocities of the disturbance, given in Table 2, were obtained using the onset times of the slope-normal displacement of rows of markers spanning the entire width of the samples. As such, these can be considered as average propagation velocities through the samples. The velocities determined for test A and B, in which slope-normal displacement was large, were somewhat higher than the velocities determined in test C and D, in which the slope-normal displacements were small in comparison (Table 2).

[34] In order to determine whether the propagation was steady state or accelerated, propagation velocities were also averaged for five subsequent markers for the calculation. With this procedure a moving average of the propagation velocity throughout the beam is determined, which is shown in Figure 9 as function of the distance to the trigger point. We note that in experiment A and B, transverse fractures through the slab occurred. It is very likely that these secondary fractures influenced the propagation velocity. Therefore, both sides of the transverse fracture were considered separately.

[35] The measured velocities in both experiments A and B, performed in samples next to each other within an hour, showed good reproducibility (Figure 9a). The propagation velocity decreased steadily in the first section of the beams from initially 60 ms^{-1} to 32 ms^{-1} in the middle section, when transverse fracture occurred. After that, the propagation velocity continued to decrease, reached a minimum of about 20 ms^{-1}, but increased again toward the far end of the sample. In experiment C the propagation velocity initially exhibited a relatively constant value of around 20 ms^{-1} and thereafter increased to 47 ms^{-1} toward the far end of the sample (Figure 9b). In experiment D the propagation velocity steadily increased from 24 ms^{-1} to 41 ms^{-1} (Figure 9c). In experiments C and D the increase in speed toward the far end was more pronounced than in experiments A and B. Steady state propagation was not observed in any of these experiments.

4. Discussion

[36] High-speed photography of fracturing weak snowpack layers demonstrates slope-normal displacements (slab subsidence) associated with fracture in accordance with theoretical expectations [*Heierli et al.*, 2008] and previous field studies [*Schweizer et al.*, 1995; *Johnson et al.*, 2004; *van Herwijnen and Jamieson*, 2005]. The present field data showed subsidence varying from case to case between 0.3 cm and 4 cm, comparable to the previously published results, which also included experiments performed with different test methods including ski cutting. This indicates that the measurements are not influenced by the test method (e.g., artificial crack from saw cut). The largest value was obtained in combination with an unusually thick layer of buried surface hoar (experiments A and B). Previously, the largest documented amplitudes were on the order of 2 cm [*van Herwijnen and Jamieson*, 2005].

[37] The crushing and volume loss of the weak layer has so far been observed in every single documented field experiment in which the displacements were accurately measured. An experiment in which the weak layer conserved its volume during fracture is yet to be documented. Even though the present field data were obtained for weak snowpack layers of finite thickness on shallow slopes, volume reduction has also been documented for so-called weak interfaces with no discernable thickness and on steeper slopes [*Schweizer et al.*, 1995; *van Herwijnen and Jamieson*, 2005; *van Herwijnen and Heierli*, 2009]. We therefore believe that

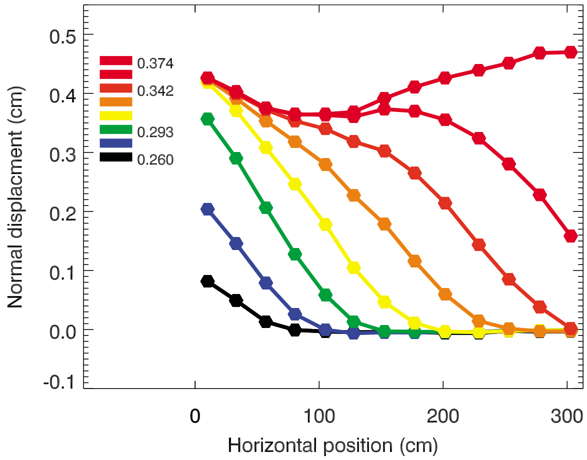

Figure 6. Snapshot of the slope-normal displacement for a row of markers in experiment D at eight different times during fracture propagation. The dots indicate the position of the markers in one row, relative to the edge of the beam where the fracture was triggered. The colors represent the time of the measurement as indicated in the legend.

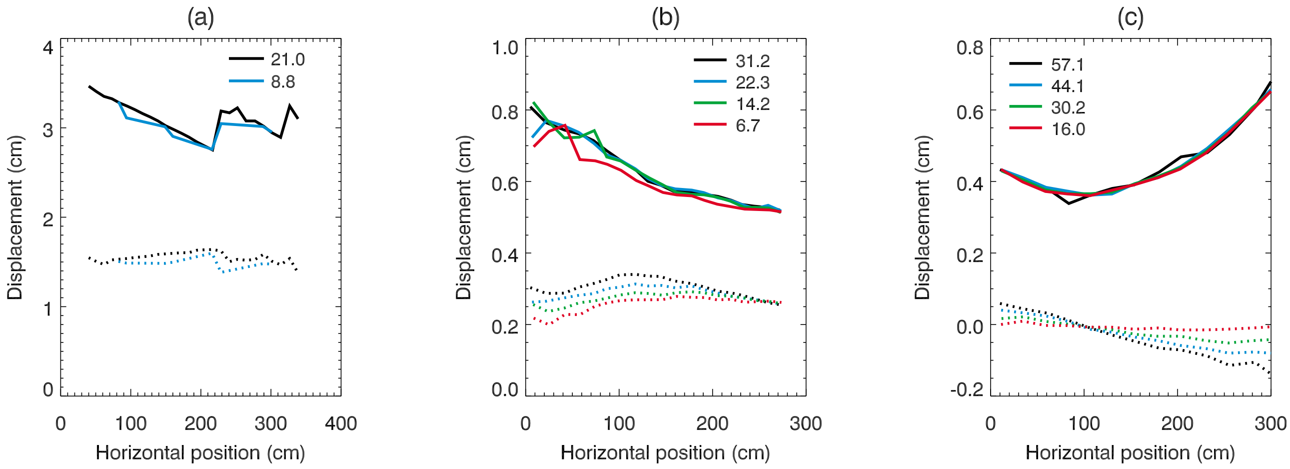

Figure 7. Final slope-parallel displacement (dashed lines) and slope-normal displacement (solid lines) as function of the distance to the edge of the beam. (a) Experiment B, (b) experiment C, and (c) experiment D. Each line represents the final displacement of one row of markers. The colors indicate the mean vertical distance in centimeters from the row of markers to the weak layer (see legend).

collapse and slab subsidence is the rule rather than the exception for fractures in a stratified snowpack. Given the highly porous and compressible nature of snow layers, this is not surprising, although the physical consequences of the volume loss have been overlooked for a long time in the modeling of slab avalanche release.

[38] The results shown in Figure 5 indicate that slope-normal and slope-parallel displacements begin simultaneously

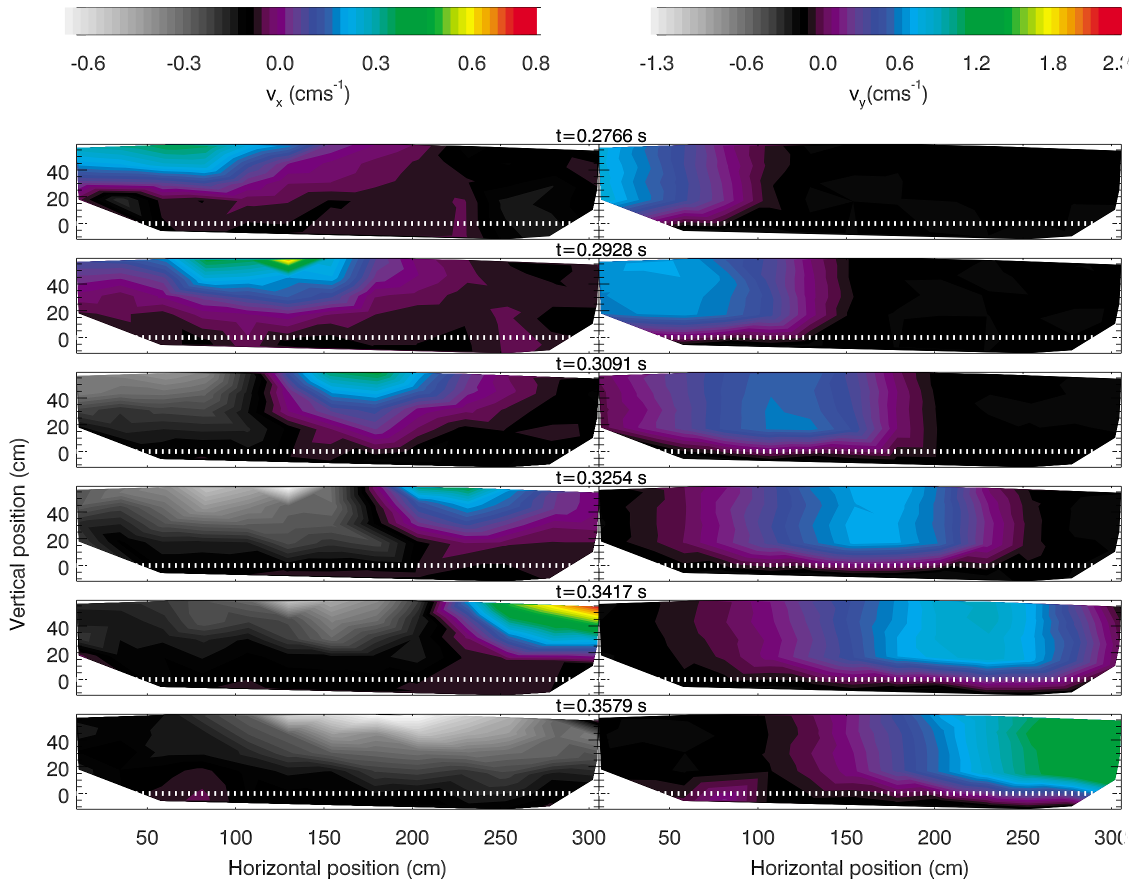

Figure 8. (left) Slope-parallel velocity (v_x) and (right) slope-normal velocity (v_x) of the markers in experiment D. Velocities are shown at six consecutive moments. The colors represent the marker velocity in cm s^{-1} as indicated in the legends. The dashed white line indicates the position of the weak layer.

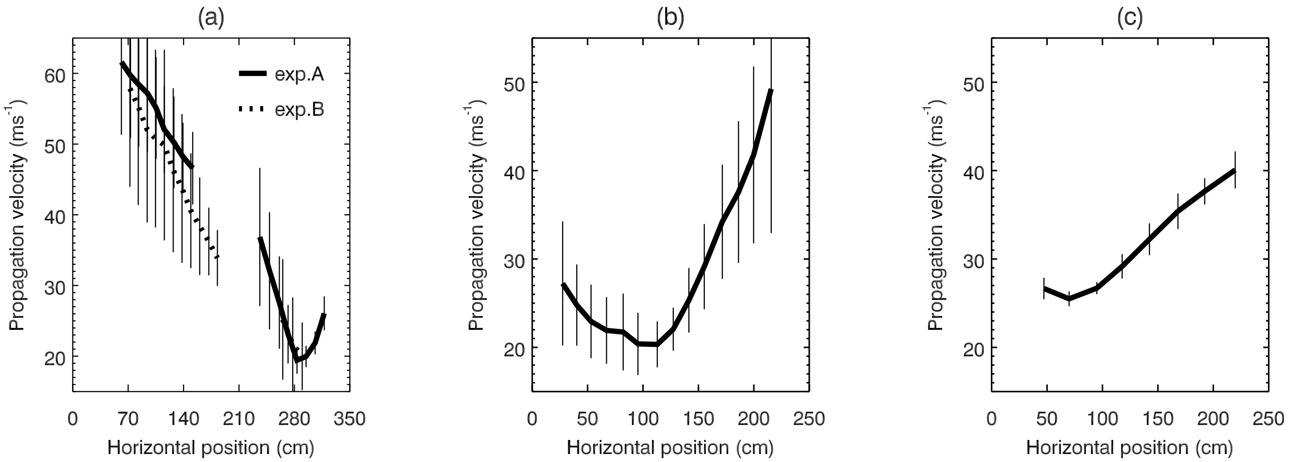

Figure 9. Propagation velocity measurements as function of position with respect to the edge of the beam where the fracture was triggered. (a) Experiments A (solid line) and B (dashed line), (b) experiment C, and (c) experiment D.

for markers close to the weak layer, where fracture occurs. We interpret this as evidence for the collapse of the weak layer structure to take place at the very crack tip, where the ice crystals composing the weak layer rearrange in a tighter packing order, as expected for anticracking. This is confirmed by the absence of any discernible shear crack traveling ahead of the collapse (Figure 8). Indeed, the slope-parallel displacements do not prevail in a zone overlapping the weak layer, as expected for shear cracks, but on the surface of the snow, as expected for bending due to the loss of slope-normal support. This view is corroborated by the equal and synchronized slope-normal motion of superposed markers (Figure 5). The results support the view that the instant crack tip is characteristic of anticracking rather than of simple shear cracking. Indeed the relative motion of the crack faces (i.e., toward each other) immediately behind the crack tip implies that work is done by the compressive load (here the pressure exerted by the weight of slab on the weak layer). Simple shear cracks, due to their volume-conserving nature, do not allow for work to be done by compressive loads.

[39] The measured mean propagation velocities associated with the collapse of the weak layer (Table 2) are in agreement with previously published values ranging from 17 to 26 ms^{-1} [*Johnson et al.*, 2004; *van Herwijnen and Jamieson*, 2005]. In the present work, the increased accuracy of the digital imaging enabled us to determine whether fracture propagation was steady state or accelerated during the experiments. The data display nonsteady state propagation but it is not clear to which cause this has to be attributed. Possible factors are the influence of free edges at both ends of the samples due to limited sample size, natural fluctuations in slab density and weak layer structure due to the disordered nature of snow or insufficient time and space to develop steady state conditions. Alternatively, steady state conditions may not or not always exist.

[40] Even though the fracture always propagated through the entire beam, the transverse fractures through the slab disrupted the fracture process in experiments A and B (Figure 7). In these two experiments the initial propagation velocity was rather high and decreased until the transverse failure occurred. Thereafter, the velocity continued to decrease to attain a minimum of about 20 ms^{-1} and increased again (Figure 9a). Since the snowpack samples A and B were artificially loaded, these velocities should be interpreted with caution. On the other hand, in experiment C the fracture propagation velocity attained a relatively stationary value of 20 ms^{-1} in the middle section of the beam (Figure 9b), possibly but not necessarily indicating steady state propagation for a brief time. In experiment D the fracture propagation velocity continuously increased, probably as a consequence of nonsteady state conditions due to finite sample size and increasing amount of collapse.

5. Conclusions

[41] A portable digital high-speed camera was used to observe the deformation field caused by fracture propagation in weak snowpack layers under field conditions. With particle tracking analysis the displacement of markers inserted above and below the weak layer was measured. A signal processing method was developed to remove artifacts due to pixel clipping which was present in some marker trajectories. As a result, the deformation field of the slab associated with the propagation of fracture through a weak layer was visualized in high detail. Slope-normal displacements ranging from approximately 0.3 cm to 4 cm were observed, in accordance with previously published measurements. In all experiments carried out in the present work and in earlier work [*van Herwijnen and Jamieson*, 2005], subsidence of the snowpack has consistently been observed. This corroborates the view that the collapse of the weak layer and subsequent subsidence of the slab is more likely the rule than the exception during slab avalanche release.

[42] High-accuracy measurements of displacement profiles manifest the propagation of a localized, wave-like disturbance associated with the volumetric collapse of the weak layer. In all experiments, the displacements immediately behind the crack tip are both in slope-normal direction (crack faces closing in) and in slope-parallel direction (crack faces slipping), the latter being always smaller in our experiments. The bending of the slab around an axis in the lower parts of the slab is evidenced by the increasing slope-

parallel displacement with increasing distance to the weak layer and by the equal slope-normal motion of any cross section of the slab.

[43] The mean propagation velocity of the collapse front ranged from 27 to 36 ms^{-1}, confirming the range of earlier measurements. Steady state propagation was not achieved, but the reasons for this are not entirely clear. The results indicate some influence of the edges due to limited sample size. In order to demonstrate steady state propagation we recommend that samples should be made at least twice as long as in the present study. Moreover, steady state propagation would require a uniform collapse height throughout the sample, a precondition which was not fulfilled in any of our experiments.

[44] Although the number of the experiments and the size of the sample is limited, a distinct pattern emerges from the analysis. The process of fracture in weak layers has presented the same fundamental characteristics of subsidence, crushing and kink-like bending for snowpacks with weak layers of different types (namely buried surface hoar layers and faceted crystals layers) and for various slope angles. The disturbance traveled with comparable velocity in all these cases. The collapse begins instantly at the crack front and is not preceded by any visible shear crack. The observation of kink-shaped bending moving directly behind the fracture front are in line with recent theoretical developments on fracture propagation in weak snowpack layers based on anticracking. The present work gives further evidence for the fundamental role of weak layer collapse and slab subsidence in the formation process of dry snow slab avalanches.

[45] **Acknowledgments.** Financial support of the European Commission under contract NEST-2005-PATH-COM-043386 and of the DFG project Gu367/30 is gratefully acknowledged. We thank Sascha Bellaire and Christoph Mitterer for their meticulous field work.

References

Canadian Avalanche Association (2002), *Observation Guidelines and Recording Standards for Weather, Snowpack and Avalanches*, Revelstoke, B. C., Canada.

Crocker, J., and D. Grier (1996), Methods of digital video microscopy for colloidal studies, *J. Colloid Interface Sci.*, *179*(1), 298–310.

Duclos, A. (1999), Déclenchement de plaques à distance, *Neige Avalanches*, *86*, 2–5.

Fletcher, R. C., and D. D. Pollard (1981), Anticrack model for pressure solution surfaces, *Geology*, *9*, 419–424.

Gauthier, D., and B. Jamieson (2006), Evaluating a prototype field test for weak layer fracture and failure propagation, paper presented at 2006 International Snow Science Workshop, Telluride, Colo.

Gauthier, D., and B. Jamieson (2008), Fracture propagation propensity in relation to snow slab avalanche release: Validating the Propagation Saw Test, *Geophys. Res. Lett.*, *35*, L13501, doi:10.1029/2008GL034245.

Gleason, J. (2004), Particle image velocimetry: A new technique to measure strain in loaded snow, paper presented at 2004 International Snow Science Workshop, Jackson Hole, Wyo.

Heierli, J. (2005), Solitary fracture waves in metastable snow stratifications, *J. Geophys. Res.*, *110*, F02008, doi:10.1029/2004JF000178.

Heierli, J., and M. Zaiser (2006), An analytical model for fracture nucleation in collapsible stratifications, *Geophys. Res. Lett.*, *33*, L06501, doi:10.1029/2005GL025311.

Heierli, J., and M. Zaiser (2008), Failure initiation in snow stratifications containing weak layers: Nucleation of whumpfs and slab avalanches, *Cold Reg. Sci. Technol.*, *52*(3), 385–400, doi:10.1016/j.coldregions.2007.02.007.

Heierli, J., P. Gumbsch, and M. Zaiser (2008), Anticrack nucleation as triggering mechanism for slab avalanches, *Science*, *321*(5886), 240–243.

Jamieson, J. B., and J. Schweizer (2000), Texture and strength changes of buried surface-hoar layers with implications for dry snow-slab avalanche release, *J. Glaciol.*, *46*, 151–160.

Johnson, B. C., J. B. Jamieson, and R. R. Stewart (2004), Seismic measurements of fracture speed in a weak snowpack layer, *Cold Reg. Sci. Technol.*, *40*(1–2), 41–45, doi:10.1016/j.coldregions.2004.05.003.

Katsman, R., and E. Aharonov (2006), A study of compaction bands originating from cracks, notches, and compacted defects, *J. Struct. Geol.*, *28*(3), 508–518, doi:10.1016/j.jsg.2005.12.007.

McClung, D. M. (1979), Shear fracture precipitated by strain softening as a mechanism of dry avalanche release, *J. Geophys. Res.*, *84*(B7), 3519–3526.

Perla, R. I., and E. R. LaChapelle (1970), A theory of snow slab failure, *J. Geophys. Res.*, *75*(36), 7619–7627.

Schweizer, J., M. Schneebeli, C. Fierz, and P. M. B. Föhn (1995), Snow mechanics and avalanche formation: Field experiments on the dynamic-response of the snow cover, *Surv. Geophys.*, *16*(5–6), 621–633.

Schweizer, J., J. B. Jamieson, and M. Schneebeli (2003), Snow avalanche formation, *Rev. Geophys.*, *41*(4), 1016, doi:10.1029/2002RG000123.

Sigrist, C., and J. Schweizer (2007), Critical energy release rates of weak snowpack layers determined in field experiments, *Geophys. Res. Lett.*, *34*, L03502, doi:10.1029/2006GL028576.

Sternlof, K. R., J. W. Rudnicki, and D. D. Pollard (2005), Anticrack inclusion model for compaction bands in sandstone, *J. Geophys. Res.*, *110*, B11403, doi:10.1029/2005JB003764.

van Herwijnen, A., and J. Heierli (2009), Measurement of crack-face friction in collapsed weak snow layers, *Geophys. Res. Lett.*, *36*, L23502, doi:10.1029/2009GL040389.

van Herwijnen, A., and B. Jamieson (2005), High-speed photography of fractures in weak snowpack layers, *Cold Reg. Sci. Technol.*, *43*(1–2), 71–82.

J. Heierli, Institut für Zuverlässigkeit von Bauteilen und Systemen, Karlsruher Institut für Technologie, Kaiserstr. 12, D-76131 Karlsruhe, Germany.

J. Schweizer and A. van Herwijnen, WSL Institute for Snow and Avalanche Research SLF, Flüelastr. 11, CH-7260 Davos-Dorf, Switzerland. (alec.van.herwijnen@gmail.com)